Materials Advances

ROYAL SOCIETY OF CHEMISTRY

COMMUNICATION

View Article Online
View Journal | View Issue

Cite this: *Mater. Adv.*, 2023, 4, 6175

Received 22nd August 2023,
Accepted 2nd November 2023

DOI: 10.1039/d3ma00576c

rsc.li/materials-advances

Plasmonic nanodendrites stabilized with autologous serum proteins for sustainable host specific photothermal tumor ablation†

Mimansa, Smriti Bansal, Pranjali Yadav and Asifkhan Shanavas *

Green synthesis of gold nanodendrites involving autologous serum proteins as both a template and stabilizer is reported. The nanodendrites, also termed as 'Plasmonic NanoSera' (PNS), with size ~150 nm, possess anisotropic dense branches with a broad extinction cross section across the visible-near infrared (I & II) regions. The PNS, with a photothermal conversion efficiency of ~58%, demonstrated significant phototoxicity in cancer cells associated with elevated intracellular reactive oxygen species. The PNS did not cause acute toxicity with intravenous administration at 20 mg kg^{-1} dosage. Intra-tumoral injection of autologous mouse serum protein-derived PNS followed by 808 nm Laser irradiation generated an ~78% higher localized temperature rise compared to a saline control in the 4T1 breast tumor model, thereby suppressing both the tumor growth and tumor burden-associated splenomegaly. This proof-of-concept study validates the preclinical safety and host-specific photothermal efficacy of PNS.

New concept

Anisotropic gold nanoparticles with a unique shape, such as nanodendrites, often require synthetic surfactants, strong reducing agents and multi-step processes for their fabrication. The present study puts forth a green route of using host-derived serum proteins as templates and stabilizers of gold nanodendrites. This approach validates a truly sustainable approach for personalized photothermal therapy. Moreover, the highly branched structure of the nanodendrites possesses a broad extinction cross-section both in the near infra-red I & II windows, allowing versatility in their photoexcitation within deep-seated tumors. Alternative to autologous serum proteins, the pH-driven method can also be utilized with commercially available pristine albumin for non-specific large-scale green synthesis of gold nanodendrites for various biomedical and catalytic applications.

1. Introduction

Gold nanoparticles are one of the most explored classes of nanomaterials in terms of diversity of shapes with appealing optical, chemical and electronic properties.[1–4] While gold nanoshells and nanorods dominated therapeutic applications, other anisotropic gold nanostructures such as nanostars, nano flowers and nanourchins with sharp, elongated branches possessing a large extinction cross-section in near infra-red (NIR) window demonstrate their promising photothermal capability due to thin branches that allow easy penetration of an electric field.[5–7] Other applications of these nanostructures are in two-photon photoluminescence imaging, computed tomographic imaging, surface-enhanced Raman scattering and photodynamic therapy.[8–11] Even though gold nanoparticles have brought about excellent opportunities for exploration, the use of synthetic surfactants and reducing agents limits their scope for *in vivo* applications.[12–14] Fabrication methods in aqueous environments involving naturally sourced biodegradable molecules such as peptides, poly nucleic acids, polymers and proteins are considered as a 'green route' and are preferred for therapeutic applications due to minimal toxicity, and marginal immunogenic response.[15–19]

Among various anisotropic morphologies that are known to possess narrow and sharp localized surface plasmon resonance, gold nanodendrites are unique for their hyperbranched structure with absorption across visible and NIR I/II regions.[20–24] The nanodendritic architecture possesses multiple arrays of branches consisting of pores with innumerable binding sites enabling applications in drug delivery and catalysis among others.[23] Prior reports have demonstrated highly branched gold nanodendrites synthesized by a seed mediated method using amphiphilic bis(amidoethyl-carbamoylethyl)-octadecylamine (C18N3) as a template.[25] Alternative to single chain C18N3 with a multi amine head, a mixture of long chain primary amines could effectively control the degree of branching of nanodendrites allowing a photothermal effect tuneable broadly within the NIR window.[23] While natural derivatives

Inorganic & Organic Nanomedicine (ION) Lab, Chemical Biology Unit, Institute of Nano Science and Technology, Sector-81, Knowledge City, Sahibzada Ajit Singh Nagar, Punjab 140306, India. E-mail: asifkhan@inst.ac.in

† Electronic supplementary information (ESI) available. See DOI: https://doi.org/10.1039/d3ma00576c

such as catechol grafted dextran have been used as a template to form gold nanodendrites, there is immense scope to circumvent the use of synthetic precursors and multi-step processes by yielding to greener routes.[26]

Our group has recently developed autologous approaches to utilize host derived serum proteins as stabilizers of drug nanocrystals and metal quantum clusters broadly termed 'NanoSera'.[27,28] Considering the established preclinical safety of this approach, in the present work we involved autologous whole serum proteins to form gold nanodendrites, also named Plasmonic-NanoSera (PNS). This rapid and seedless one pot synthesis allows serum proteins to serve as both a template and stabilizer of the nanodendrites. We observed that PNS with adequate photothermal conversion efficiency could aid in localized ablation of syngeneic 4T1 breast tumors in Balb/c mice.

2. Results and discussion

2.1. Synthesis and characterization of Plasmonic-NanoSera (PNS)

We developed a simple one-pot green synthetic method involving whole serum proteins as a template for the fabrication of PNS with dendritic morphology (Fig. 1a). As an initial proof of concept in terms of method optimization, characterization and *in vitro* experiments, PNS was synthesized from fetal bovine serum (FBS) and for preclinical assessment it was synthesized from autologous mouse serum (MS). Serum proteins predominantly possess alpha helical conformation (Fig. 1c) and have an overall isoelectric pH (IEP) of ~4.5 (Fig. S1, ESI†). Their exposure to $HAuCl_4$ leads to a drop in pH to ~2.6. This imparts an overall positive charge leading to electrostatic interactions between the serum proteins and tetrachloroaurate.

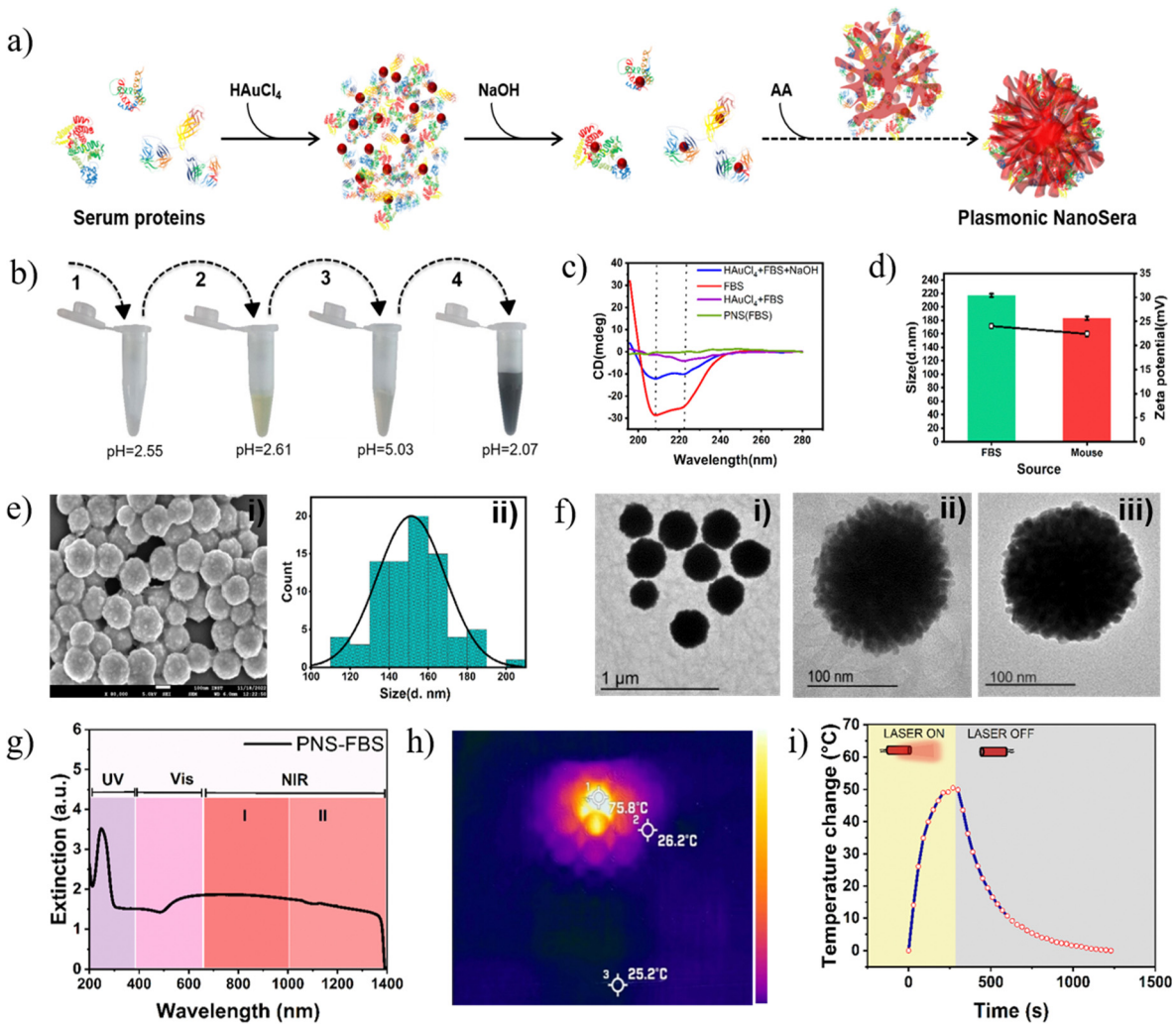

Fig. 1 Synthesis and characterization of PNS. (a) Schematic representation of Plasmonic NanoSera synthesized from whole serum proteins; (b) appearance of the reaction mixture after the addition of FBS (1), $HAuCl_4$ (2), NaOH (3) and AA (4); (c) CD spectra of the sample after the addition of different components; (d) hydrodynamic size and zeta potential of PNS synthesized from FBS and MS; (e) FESEM (i) and particle size distribution (ii) of PNS–FBS; (f) TEM images of PNS–HS (human serum) (i) and (ii) and PNS–MS (iii); (g) UV-Vis-NIR extinction spectra of PNS–FBS; (h) thermal image of PNS–FBS irradiated with a NIR laser (808 nm, 2 W) for 5 min (1 – PNS, 2 – water and 3 – room temperature); (i) photothermal change of PNS from room temperature.

This interaction as well results in a substantial decrease in alpha helical structure (Fig. 1c) yielding a yellow turbid solution (Fig. 1b). Subsequently, with the addition of NaOH, the pH elevates to ~5 turning the solution colourless (Fig. 1b) due to the dissociation of chloride ions. At this pH, the proteins partially regain their structure with the disappearance of the turbidity. This snap between conformation allows trapping of aurate ions within the proteins and subsequently acts as multiple nucleation centres for its further reduction to Au^0 with the addition of ascorbic acid leading to the formation of a uniformly sized gold nanodendritic structure. Since one ascorbic acid molecule can contribute 2 electrons for Au^{3+} reduction in $AuCl_4^-$, the role of ascorbic acid to gold chloride ratio must be higher than 3 : 2. This ratio plays a critical role as an increase in ascorbic acid leads to augmented reduction of gold ions.[19] In the absence of NaOH, the direct addition of ascorbic acid to the protein–tetrachloroaurate solution leads to hyper acidification causing inhomogeneous precipitation of the proteins resulting in polydispersed and unstable gold nanoparticles (Fig. S2, ESI†). Post synthesis, the oxidation state of gold in the PNS was confirmed by XPS analysis, where characteristic peaks of Au^0 were observed at 83.7 eV and 87.3 eV (Fig. S3, ESI†).[29] PNS prepared from FBS and MS possessed a hydrodynamic size of 217.2 ± 2.45 & 183.1 ± 2.6 and zeta potential of 24.03 ± 0.55 and 22.4 ± 0.62, respectively (Fig. 1d).

The external morphology of monodispersed spherical PNS showed a non-smooth surface (Fig. 1e, (i)) as observed under FESEM with particle size averaging around 150 nm (Fig. 1e, ii). TEM of PNS–FBS (Fig. 1f, (i) and (ii)) and PNS–MS (Fig. 1f, (iii)) showed radially protruding branches typical of anisotropic nanodendrites. These dendritic structures allow the PNS to have a broad extinction cross section across the visible-near infrared (I & II) regions from 500 nm to 1350 nm (Fig. 1g).[30] Plasmonic nanodendrites have been reported to possess exceptional photothermal transduction efficiency. PNS–FBS upon 808 nm Laser exposure generated an ~50 °C temperature rise from RT with a photothermal conversion efficiency (PCE) of 58.3% (Fig. 1h and Fig. S1, ESI†). Post irradiation, while the spectral pattern was mostly preserved, there was an overall decrease in the absorbance by 22%, probably due to the effect of irradiation on the colloidal stability (Fig. S5, ESI†). Considering the broad visible light absorption of PNS, the PCE under white light irradiation was also measured and observed to be only 0.57% (Fig. S6, ESI†). This implies that PNS can be specifically used for localized hyperthermia with a NIR Laser without any off-target effect due to visible light.

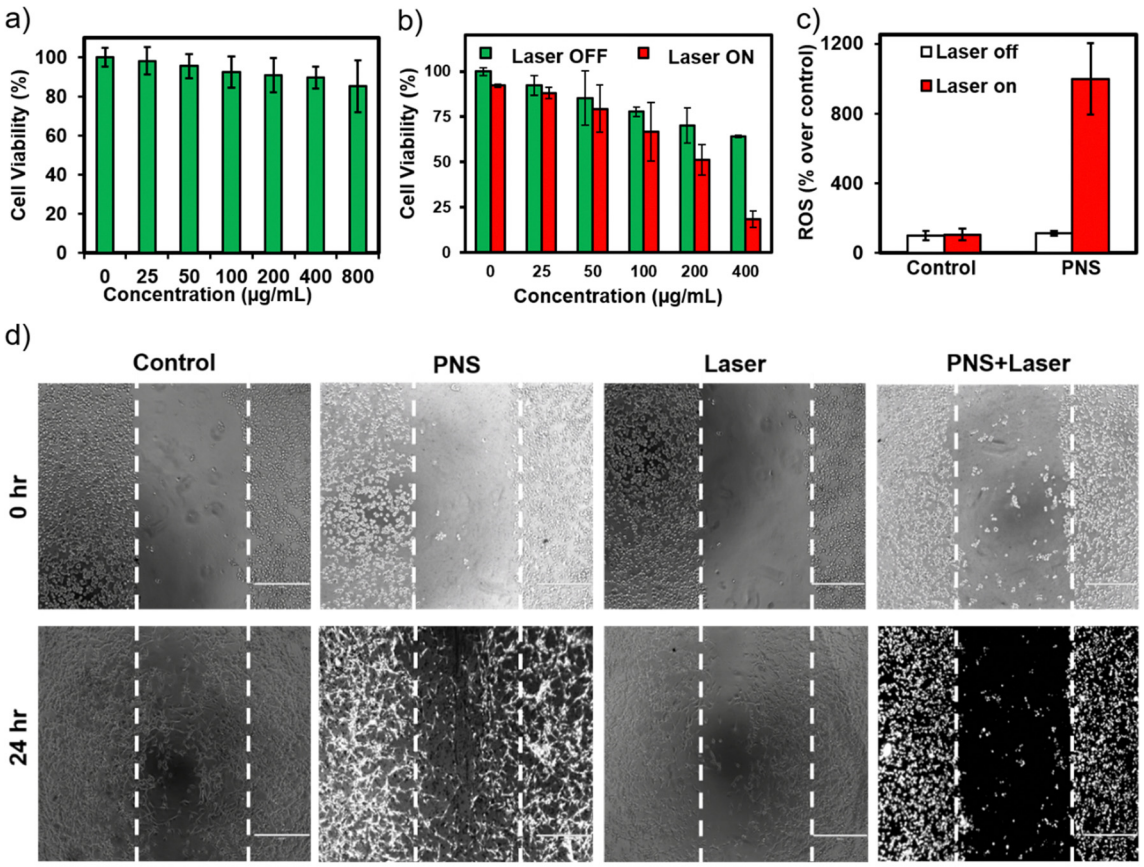

Fig. 2 Biocompatibility and Anticancer activity. (a) Biocompatibility of PNS for 24 hours in fibroblast cells; (b) anticancer activity of PNS in the presence and absence of Laser irradiation; (c) percentage intracellular ROS post treatment with 400 μg mL^{-1} of PNS and 5 min laser exposure; (d) cancer cell migration in the presence and absence of photothermal therapy (PNS-treated cells show enhanced contrast from background due to scattering from gold).

Furthermore, SDS-PAGE analysis revealed predominance of albumin in the proteins extracted from PNS as shown in Fig. S7 (ESI†). This observation prompted us to adapt the synthetic method with only bovine serum albumin. FESEM and TEM images of albumin-derived gold nanoparticles showed a similar anisotropic structure to that of PNS from FBS, HS and MS (Fig. S8 and S9, ESI†). Elemental mapping also confirmed the presence of gold and nitrogen, the latter being from serum proteins (Fig. S10, ESI†). These observations indicate that while PNS enables host specific photothermal therapy, albumin can be explored for non-specific large-scale green synthesis of gold nanodendrites for various biomedical and catalytic applications.

2.2. Biocompatibility and anticancer activity

PNS was found to be biocompatible for concentrations up to 800 μg mL^{-1} against fibroblast cells (L929) with ≥80% cell viability (Fig. 2a). In the absence of laser irradiation, higher concentrations of PNS caused a decrease in the number of viable breast cancer cells in comparison to the control (Fig. 2b). It is known that high surface curvatures on nanoparticles associate stronger with the plasma membrane due to discrete points of contact compared to their spherical counterparts.[31] Nanomechanical signatures of cancer cells include low membrane stiffness that make them more susceptible to damage compared to normal cells.[32–34] Furthermore, a concentration dependent photothermally induced anticancer activity was observed with PNS at 400 μg mL^{-1} concentration incurring high intracellular reactive oxygen species over control cells (Fig. 2c). Similar concentration of PNS in the presence of a laser significantly inhibited breast cancer cell migration, affecting the overall morphology of the cells in comparison to other groups (Fig. 2d). An effective photothermal activity in cells encouraged preclinical evaluation of PNS fabricated using pooled autologous mouse serum proteins.

2.3. Preclinical safety assessment and host specific photothermal therapy

Acute safety studies were performed post 24 hours of PNS-MS administration *via* an intravenous route. Liver, kidney and

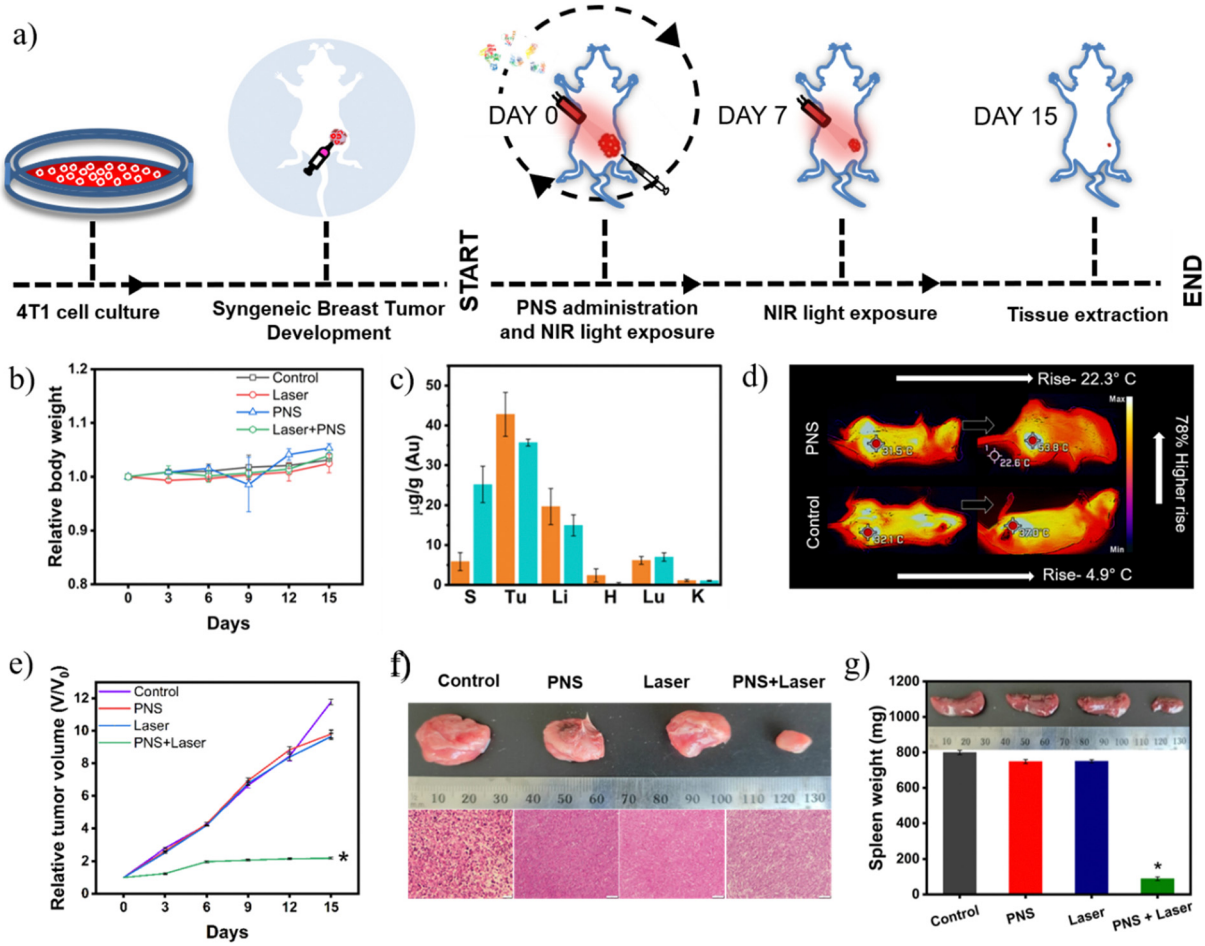

Fig. 3 Host specific photothermal therapy. (a) PNS dosage and laser irradiation regime; (b) relative body weight recorded for a period of 15 days in different groups; (c) gold content in major organs (Li – liver; Tu – tumor; S – spleen; H – heart; Lu – lung; K – kidney) at day 1 (orange column) and day 8 (blue column) of the study; (d) thermal images of representative mice in the PNS and control groups pre & post 5 min laser exposure; (e) tumor regression profile; (f) size and histological analysis of the tumor from different groups; (g) weight and size of the spleen from different groups post 15 days treatment (n = 3; *$p \leq 0.05$, **$p \leq 0.01$, ***$p \leq 0.001$).

heart functions were assessed by evaluating respective serum markers. All markers such as creatinine, blood urea nitrogen, aspartate aminotransferase, alanine transaminase and troponin-I were found to be within the normal range (Fig. S11, ESI†). Additionally, histological analysis of the heart, kidneys, lungs, liver and spleen post day 1 of PNS-MS intravenous injection revealed no signs of inflammation or degeneration (Fig. S12, ESI†). Furthermore, PNS-MS fabricated using pooled autologous serum proteins from 4T1 tumor bearing in-bred Balb/c mice were assessed for host specific photothermal therapy.

Fig. 3a shows the timeline of the syngeneic 4T1 breast tumor generation, dosage and regression analysis over 15 days. Overall health of the mice was assessed by relative body weight in different groups and found to be normal throughout the study as depicted in Fig. 3b. Two doses of Laser irradiation for 5 minutes were administered at day 0 and day 7. To assess the systemic spillover of the PNS post irradiation, elemental analysis of gold at day 1 and day 8 was performed. It was observed that gold was present in the spleen, liver and lungs at day 1, where the content further increased in the spleen at day 8 (Fig. 3c). The presence of gold in these organs indicates that the photothermal ablation could damage the tumor vasculature and allow PNS to enter systemic circulation followed by ingression into the other organs. The tumor microenvironment is typically abundant with proteinases that trigger protein catabolism.[35] The degradation of proteins associated with PNS was confirmed with exposure of the intricate pores in the PNS as seen in TEM (Fig. S13, ESI†).

Intratumoral administration of PNS-MS followed by 808 nm Laser irradiation imparted a localized temperature rise of $\sim$22 °C above the physiological temperature. However, the saline control irradiated under similar conditions caused only an $\sim$5 °C temperature rise as shown in (Fig. 3d). Significant tumor suppression was observed in the photothermal therapy group owing to localized ablation (Fig. 3e). In contrast to this, an $\sim$10-fold increase in tumor growth over the study period was observed in the control groups. This also implies that both PNS and Laser irradiation could synergistically inhibit tumor growth over a period of 15 days. Further histological examination of the tumor microstructures at the end of the study revealed significant necrosis in the photothermal group in contrast to the highly viable tumor mass in control groups (Fig. 3f).[36] A hyperactivated immune response due to tumor antigens causes splenomegaly in tumor bearing mice.[37] PNS-mediated personalized photothermal therapy by inhibiting tumor growth allowed retention of spleen weight in the normal range (Fig. 3g). However, the control groups showed significantly enlarged spleens due to the associated tumor burden. These observations warrant further exploration of PNS as a viable personalized nanotransducer for photothermal therapy.

3. Conclusion

Near infrared light absorbing plasmonic nanoparticles are considered a unique and strong class of photothermal agents for ablating solid tumors. However, the reaction components utilized for fabricating them require careful consideration for *in vivo* administration and safety. We have conceptually demonstrated a sustainable method involving autologous serum proteins for the synthesis of anisotropic gold nanodendrites having localized surface plasmon tuneable across the NIR I & II windows. Plasmonic NanoSera fabricated from autologous tumor-bearing mouse derived serum proteins were found to generate a significant photothermal effect localized to the tumor tissue. Albumin was found to be the major protein contributing to the nanodendrite formation. Thus, the approach can also be applied with commercial pristine albumin for generic large-scale green synthesis of gold nanodendrites. Moreover, post synthetic enzymatic removal of the proteins from the nanodendrites exposes the intricate pores within the branched structure where therapeutic cargo such as small molecules can be seamlessly loaded for diversified nano medicinal approaches.

4. Materials and methods

4.1. Synthesis

A one-pot synthesis was carried out in a vial, in which different components were added in a series of 5 mM $HAuCl_4$ to 10 mg mL^{-1} of fetal bovine serum (FBS) or mouse serum (MS) followed by 100 mM NaOH and then 100 mM ascorbic acid. The volume was made up to 1000 μL and after gentle mixing centrifuged at 5000 rpm for 5 min. The supernatant was discarded and the pellet was redispersed into water and sonicated (GT SONIC ultrasonic cleaner) until redissolved.

4.2. Characterization

Size and zeta potential were attained with a Zetasizer (Malvern, U.K.). A JEM 2100 (JEOL, Japan) operating at 200 kV was used to acquire transmission electron microscope (TEM) images of the nanoparticles and a JEOL JSM-7610FPlus for FESEM. The particle size distribution was done by using ImageJ software. Conformational changes of proteins during synthesis steps were evaluated using a JASCO J-1500 CD spectrometer. Extinction spectra of PNS in the UV-Vis-NIR were recorded from 200 to 1400 nm (Agilent Cary-5000). The oxidation state of PNS was measured with X-ray photoelectron spectroscopy (Thermo k-alpha). Proteins extracted from PNS were resolved in 12% polyacrylamide gel and visualized with Coomassie brilliant blue staining (Biorad ChemiDoc XRS).

4.3. Photothermal conversion efficiency

The photothermal conversion efficiency of the 400 μg mL^{-1} solution was measured by irradiating the sample with an 808 nm Laser at 2 W for 5 minutes and a xenon arc lamp at 450 W for 5 minutes. Temperature changes were recorded for 10 minutes (Laser ON-5 min, Laser OFF-5 min) with an FLIR One thermal imaging camera. Photothermal conversion

efficiency was calculated using the below formula following previously reported methods.[38,39]

$$\eta = \frac{hs(T_{max} - T_{surr}) - Q_{diss}}{I(1 - 10^{-A808})}$$

4.4. MTT assay

Plasmonic-NanoSera (PNS) was tested on 4T1 breast cancer cells and L929 fibroblast cells using an MTT (3-(4,5-dimethylthiazol-2-yl)-2,5-diphenyl tetrazolium bromide) assay. Cells were seeded at a density of 4×10^3 cells per well and incubated at 37 °C under 5% CO_2 for 24 hours. For biocompatibility, cells were then treated with PNS at different concentrations (0 to 800 μg mL^{-1}) and for the anticancer effect, PNS was treated at the same concentration range with a 5 minutes exposure session of the laser (2 W, 808 nm). Post treatment MTT was incubated for 4 hours followed by DMSO and the absorbance was recorded at 590 nm.

$$\text{Cell viability \%} = \frac{\text{absorbance of the treated cells}}{\text{absorbance of the control cells}} \times 100$$

4.5. Cell migratory assay

A fully confluent 96 well plate was subjected to a wound with a 200 μL microtip and further washed with PBS to remove free floating cell debris. The cells were then treated with PNS, laser alone, or PNS + laser at 400 μg mL^{-1} for 24 hours and imaged using an inverted microscope.

4.6. Reactive oxygen species (ROS) assay

4T1 cells were seeded at a density of 2.5×10^5 cells per well for the control and treated with 400 μg mL^{-1} PNS + 5 min Laser exposure. Post treatment cells were incubated with H_2DCFDA for 60 minutes at 37 °C. Measurements were recorded following excitation at 488 nm and emission at 535 nm using a Bio Tek plate reader.

4.7. Animal housing and dosing

4- to 8-week-old, female C57BL/6 and Balb/c mice were used for preclinical and PTT studies respectively with approval from the institute of animal ethics committee of IISER Mohali (IISERM/SAFE/PRT/2020/001). Animals were housed in individually vented cages and acclimatized for two weeks before starting the experiments. Mice were randomly assigned to four major groups having three mice each.

Group 1-Control: mice injected intratumorally with 100 μL PBS.

Group 2-PNS: mice injected intratumorally with 100 μL PNS.

Group 3-Laser: mice injected intratumorally with 100 μL PBS with 5 minutes of laser irradiation.

Group 4-PNS + Laser: mice injected intratumorally with 100 μL PNS with 5 minutes of laser irradiation.

4.8. Serum biomarker analysis

An acute response by the vital organs is assessed by the quantitative colorimetric ERBA kits, measuring the standard serum markers post day 1 of injection. A qualitative lateral flow test kit by standard diagnostics, Inc. was used to evaluate serum Troponin I level, a single band indicating ≤ 0.5 ng mL^{-1} or a double band > 0.5 ng mL^{-1}.

4.9. Tumor development and PTT

A 4T1 syngenic mouse model was developed by subcutaneously injecting 8 million cells into the mammary fat pad of female Balb/c mice. PNS was synthesized using serum retrieved from 125 mm^3 palpable tumor bearing mice. *In vivo* PTT efficiency was evaluated after intratumorally injecting PNS and irradiating with an 808 nm laser for 5 minutes. Temperature changes were recorded with a thermal imaging camera (FLIR One Pro). Laser exposure was given twice on day 0 at 1 hour post intratumoral injection and on day 7 of the study. The change in tumor volume was monitored with a vernier calliper at every third day of the study along with the body weight of the animal. The spleen and tumor were excised on the 15th day for histological analysis and signs of splenomegaly.

4.10. Tissue analysis

Histopathological analysis of the liver, lungs, kidneys, heart, spleen and tumor was performed for preclinical study and host specific photothermal therapy. The organs were excised and fixed in 10% neutral buffer formalin. A 5 μm thin section of the organs embedded in paraffin wax was stained with haematoxylin and eosin dye and examined under an Olympus light microscope.

4.11. ICP-MS

Tumor, spleen, liver, heart, lungs and kidneys were excised at day 1, day 8 and day 15 of the host specific study. Organs were treated with ICP-MS grade HNO_3 at 60 °C until digested. Samples were then diluted with deionized water and analysed using inductively coupled plasma mass spectrometry (Thermo Fisher K-Alpha).

4.12. Statistical analysis

All data points were recorded in triplicate and indicated as mean with standard deviation (mean ± standard deviation). One-way ANOVA and a two tailed *t*-test was performed for significance ($*p \leq 0.05$, $**p \leq 0.01$, $***p \leq 0.001$).

Author contributions

Mimansa: methodology, visualization, data curation, formal analysis, investigation, and writing original draft. Smriti Bansal: methodology, investigation and formal analysis. Pranjali Yadav: methodology, investigation and formal analysis. Asifkhan Shanavas: conceptualization, project administration, supervision, resources, visualization, review and editing of manuscript.

Conflicts of interest

There is no conflict of interest among the authors.

Acknowledgements

Ms Mimansa sincerely acknowledges University Grants Commission (UGC) for providing a doctoral fellowship. Dr Asifkhan Shanavas sincerely acknowledges Prof. Reena Das and Dr Manu Jamwal at the Department of Hematology, PGIMER Chandigarh, for assisting in obtaining Institute Ethics Committee approval (Approval No. PGI/IEC/2020/000787) for utilizing human serum in the study.

References

1 J. Piella, N. G. Bastús and V. Puntes, Size-Controlled Synthesis of Sub-10-Nanometer Citrate-Stabilized Gold Nanoparticles and Related Optical Properties, *Chem. Mater.*, 2016, **28**(4), 1066–1075, DOI: **10.1021/acs.chemmater.5b04406**.

2 S. Helmi, C. Ziegler, D. J. Kauert and R. Seidel, Shape-Controlled Synthesis of Gold Nanostructures Using DNA Origami Molds, *Nano Lett.*, 2014, **14**(11), 6693–6698, DOI: **10.1021/nl503441v**.

3 A. K. Samal, L. Polavarapu, S. Rodal-Cedeira, L. M. Liz-Marzán, J. Pérez-Juste and I. Pastoriza-Santos, Size Tunable Au@Ag Core–Shell Nanoparticles: Synthesis and Surface-Enhanced Raman Scattering Properties, *Langmuir*, 2013, **29**(48), 15076–15082, DOI: **10.1021/la403707j**.

4 U. S. Demir, R. Shahbazi, S. Calamak, S. Ozturk, M. Gultekinoglu and K. Ulubayram, Gold Nano-Decorated Aligned Polyurethane Nanofibers for Enhancement of Neurite Outgrowth and Elongation: GOLD NANO-DECORATED ALIGNED PU NANOFIBERS, *J. Biomed. Mater. Res.*, 2018, **106**(6), 1604–1613, DOI: **10.1002/jbm.a.36365**.

5 J. Xie, Q. Zhang, J. Y. Lee and D. I. C. Wang, The Synthesis of SERS-Active Gold Nanoflower Tags for *In Vivo* Applications, *ACS Nano*, 2008, **2**(12), 2473–2480, DOI: **10.1021/nn800442q**.

6 O. M. Bakr, B. H. Wunsch and F. Stellacci, High-Yield Synthesis of Multi-Branched Urchin-Like Gold Nanoparticles, *Chem. Mater.*, 2006, **18**(14), 3297–3301, DOI: **10.1021/cm060681i**.

7 H. Yuan, C. G. Khoury, H. Hwang, C. M. Wilson, G. A. Grant and T. Vo-Dinh, Gold Nanostars: Surfactant-Free Synthesis, 3D Modelling, and Two-Photon Photoluminescence Imaging, *Nanotechnology*, 2012, **23**(7), 075102, DOI: **10.1088/0957-4484/23/7/075102**.

8 H. Wang, T. B. Huff, D. A. Zweifel, W. He, P. S. Low, A. Wei and J.-X. Cheng, *In Vitro* and *in Vivo* Two-Photon Luminescence Imaging of Single Gold Nanorods, *Proc. Natl. Acad. Sci. U. S. A.*, 2005, **102**(44), 15752–15756, DOI: **10.1073/pnas.0504892102**.

9 C. P. Scotson, M. Munoz-Hernando, S. J. Duncan, S. A. Ruiz, S. D. Keyes, A. van Veelen, I. E. Dunlop and T. Roose, Stabilizing Gold Nanoparticles for Use in X-Ray Computed Tomography Imaging of Soil Systems, *R. Soc. open sci.*, 2019, **6**(10), 190769, DOI: **10.1098/rsos.190769**.

10 Y. Hu, H. Cheng, X. Zhao, J. Wu, F. Muhammad, S. Lin, J. He, L. Zhou, C. Zhang, Y. Deng, P. Wang, Z. Zhou, S. Nie and H. Wei, Surface-Enhanced Raman Scattering Active Gold Nanoparticles with Enzyme-Mimicking Activities for Measuring Glucose and Lactate in Living Tissues, *ACS Nano*, 2017, **11**(6), 5558–5566, DOI: **10.1021/acsnano.7b00905**.

11 X. Wei, H. Chen, H. P. Tham, N. Zhang, P. Xing, G. Zhang and Y. Zhao, Combined Photodynamic and Photothermal Therapy Using Cross-Linked Polyphosphazene Nanospheres Decorated with Gold Nanoparticles, *ACS Appl. Nano Mater.*, 2018, **1**(7), 3663–3672, DOI: **10.1021/acsanm.8b00776**.

12 A. Shiohara, J. Langer, L. Polavarapu and L. M. Liz-Marzán, Solution Processed Polydimethylsiloxane/Gold Nanostar Flexible Substrates for Plasmonic Sensing, *Nanoscale*, 2014, **6**(16), 9817–9823, DOI: **10.1039/C4NR02648A**.

13 M. Schütz, D. Steinigeweg, M. Salehi, K. Kömpe and S. Schlücker, Hydrophilically Stabilized Gold Nanostars as SERS Labels for Tissue Imaging of the Tumor Suppressor P63 by Immuno-SERS Microscopy, *Chem. Commun.*, 2011, **47**(14), 4216, DOI: **10.1039/c0cc05229a**.

14 H.-Y. Wu, M. Liu and M. H. Huang, Direct Synthesis of Branched Gold Nanocrystals and Their Transformation into Spherical Nanoparticles, *J. Phys. Chem. B*, 2006, **110**(39), 19291–19294, DOI: **10.1021/jp063711d**.

15 E. A. Egorova, M. M. J. van Rijt, N. Sommerdijk, G. S. Gooris, J. A. Bouwstra, A. L. Boyle and A. Kros, One Peptide for Them All: Gold Nanoparticles of Different Sizes Are Stabilized by a Common Peptide Amphiphile, *ACS Nano*, 2020, **14**(5), 5874–5886, DOI: **10.1021/acsnano.0c01021**.

16 J. Shin, X. Zhang and J. Liu, DNA-Functionalized Gold Nanoparticles in Macromolecularly Crowded Polymer Solutions, *J. Phys. Chem. B*, 2012, **116**(45), 13396–13402, DOI: **10.1021/jp310662m**.

17 M. K. Corbierre, N. S. Cameron, M. Sutton, S. G. J. Mochrie, L. B. Lurio, A. Rühm and R. B. Lennox, Polymer-Stabilized Gold Nanoparticles and Their Incorporation into Polymer Matrices, *J. Am. Chem. Soc.*, 2001, **123**(42), 10411–10412, DOI: **10.1021/ja0166287**.

18 A. Housni, M. Ahmed, S. Liu and R. Narain, Monodisperse Protein Stabilized Gold Nanoparticles *via* a Simple Photochemical Process, *J. Phys. Chem. C*, 2008, **112**(32), 12282–12290, DOI: **10.1021/jp803890a**.

19 S. Sasidharan, D. Bahadur and R. Srivastava, Protein-Poly(Amino Acid) Nanocore–Shell Mediated Synthesis of Branched Gold Nanostructures for Computed Tomographic Imaging and Photothermal Therapy of Cancer, *ACS Appl. Mater. Interfaces*, 2016, **8**(25), 15889–15903, DOI: **10.1021/acsami.6b03428**.

20 S. E. Skrabalak, J. Chen, Y. Sun, X. Lu, L. Au, C. M. Cobley and Y. Xia, Gold Nanocages: Synthesis, Properties, and Applications, *Acc. Chem. Res.*, 2008, **41**(12), 1587–1595, DOI: **10.1021/ar800018v**.

21 N. G. Bastús, J. Comenge and V. Puntes, Kinetically Controlled Seeded Growth Synthesis of Citrate-Stabilized Gold Nanoparticles of up to 200 Nm: Size Focusing versus Ostwald Ripening, *Langmuir*, 2011, **27**(17), 11098–11105, DOI: **10.1021/la201938u**.

22 X. Ye, L. Jin, H. Caglayan, J. Chen, G. Xing, C. Zheng, V. Doan-Nguyen, Y. Kang, N. Engheta, C. R. Kagan and

C. B. Murray, Improved Size-Tunable Synthesis of Monodisperse Gold Nanorods through the Use of Aromatic Additives, *ACS Nano*, 2012, **6**(3), 2804–2817, DOI: **10.1021/nn300315j**.

23 A. O. Oladipo, T. T. I. Nkambule, B. B. Mamba and T. A. M. Msagati, Therapeutic Nanodendrites: Current Applications and Prospects, *Nanoscale Adv.*, 2020, **2**(11), 5152–5165.

24 J. Sun, J. Wang, W. Hu, Y. Wang, T. Chou, Q. Zhang, B. Zhang, Z. Yu, Y. Yang, L. Ren and H. Wang, Camouflaged Gold Nanodendrites Enable Synergistic Photodynamic Therapy and NIR Biowindow II Photothermal Therapy and Multimodal Imaging, *ACS Appl. Mater. Interfaces*, 2021, **13**(9), 10778–10795, DOI: **10.1021/acsami.1c01238**.

25 W. Jia, J. Li and L. Jiang, Synthesis of Highly Branched Gold Nanodendrites with a Narrow Size Distribution and Tunable NIR and SERS Using a Multiamine Surfactant, *ACS Appl. Mater. Interfaces*, 2013, **5**(15), 6886–6892, DOI: **10.1021/am401006b**.

26 H. Y. Son, K. R. Kim, C. A. Hong and Y. S. Nam, Morphological Evolution of Gold Nanoparticles into Nanodendrites Using Catechol-Grafted Polymer Templates, *ACS Omega*, 2018, **3**(6), 6683–6691, DOI: **10.1021/acsomega.8b00538**.

27 Mimansa, M. Jamwal, R. Das and A. Shanavas, High Drug Loading Nanoparticles Stabilized with Autologous Serum Proteins Passively Inhibits Tumor Growth, *Biomacromolecules*, 2022, **23**(12), 5065–5073, DOI: **10.1021/acs.biomac.2c00907**.

28 K. Sood, P. Yadav, M. Jamwal, R. Das and A. Shanavas, Preclinical Safety Assessment of Photoluminescent Metal Quantum Clusters Stabilized with Autologous Serum Proteins for Host Specific Theranostics, *Nanotheranostics*, 2023, **7**(3), 316–326, DOI: **10.7150/ntno.82978**.

29 P. Jiang, S. Xie, J. Yao, S. He, H. Zhang, D. Shi, S. Pang and H. Gao, Two-Dimensional Self-Organization of 1-Nonanethiol-Capped Gold Nanoparticles, *Chin. Sci. Bull.*, 2001, **46**(12), 996–998, DOI: **10.1007/BF03183543**.

30 P. Qiu, M. Yang, X. Qu, Y. Huai, Y. Zhu and C. Mao, Tuning Photothermal Properties of Gold Nanodendrites for in Vivo Cancer Therapy within a Wide near Infrared Range by Simply Controlling Their Degree of Branching, *Biomaterials*, 2016, **104**, 138–144, DOI: **10.1016/j.biomaterials.2016.06.033**.

31 S. Dasgupta, T. Auth and G. Gompper, Shape and Orientation Matter for the Cellular Uptake of Nonspherical Particles, *Nano Lett.*, 2014, **14**(2), 687–693, DOI: **10.1021/nl403949h**.

32 S. E. Cross, Y.-S. Jin, J. Rao and J. K. Gimzewski, Nanomechanical Analysis of Cells from Cancer Patients, *Nat. Nanotechnol.*, 2007, **2**(12), 780–783, DOI: **10.1038/nnano.2007.388**.

33 A. Stylianou, C. Voutouri, F. Mpekris and T. Stylianopoulos, Pancreatic Cancer Presents Distinct Nanomechanical Properties During Progression, *Ann. Biomed. Eng.*, 2023, **51**(7), 1602–1615, DOI: **10.1007/s10439-023-03168-3**.

34 *The nanomechanical signature of breast cancer | Nature Nanotechnology*. **https://www.nature.com/articles/nnano.2012.167** (accessed 2023-06-04).

35 N. Zhang, F. Zhao, Q. Zou, Y. Li, G. Ma and X. Yan, Multi-triggered Tumor-Responsive Drug Delivery Vehicles Based on Protein and Polypeptide Coassembly for Enhanced Photodynamic Tumor Ablation, *Small*, 2016, **12**(43), 5936–5943, DOI: **10.1002/smll.201602339**.

36 C. Chen, Z. Nong, Q. Xie, J. He, W. Cai, X. Tang, X. Chen, R. Huang and Y. Gao, 2-Dodecyl-6-Methoxycyclohexa-2,5-Diene-1,4-Dione Inhibits the Growth and Metastasis of Breast Carcinoma in Mice, *Sci. Rep.*, 2017, **7**(1), 6704, DOI: **10.1038/s41598-017-07162-3**.

37 S. A. duPre' and K. W. Hunter, Murine Mammary Carcinoma 4T1 Induces a Leukemoid Reaction with Splenomegaly: Association with Tumor-Derived Growth Factors, *Exp. Mol. Pathol.*, 2007, **82**(1), 12–24, DOI: **10.1016/j.yexmp.2006.06.007**.

38 X. Liu, B. Li, F. Fu, K. Xu, R. Zou, Q. Wang, B. Zhang, Z. Chen and J. Hu, Facile Synthesis of Biocompatible Cysteine-Coated CuS Nanoparticles with High Photothermal Conversion Efficiency for Cancer Therapy, *Dalton Trans.*, 2014, **43**(30), 11709.

39 Q. Tian, F. Jiang, R. Zou, Q. Liu, Z. Chen, M. Zhu, S. Yang, J. Wang, J. Wang and J. Hu, Hydrophilic Cu_9S_5 Nanocrystals: A Photothermal Agent with a 25.7% Heat Conversion Efficiency for Photothermal Ablation of Cancer Cells *in Vivo*, *ACS Nano*, 2011, **5**(12), 9761–9771, DOI: **10.1021/nn203293t.**.